



Quantum Nondemolition Dispersive Readout of a Superconducting Artificial Atom Using Large Photon Numbers

Daria Gusenkova, Martin Spiecker, Richard Gebauer, Madita Willsch, Dennis Willsch, Francesco Valenti, Nick Karcher, Lukas Grünhaupt, Ivan Takmakov, Patrick Winkel, et al.

► To cite this version:

Daria Gusenkova, Martin Spiecker, Richard Gebauer, Madita Willsch, Dennis Willsch, et al.. Quantum Nondemolition Dispersive Readout of a Superconducting Artificial Atom Using Large Photon Numbers. *Physical Review Applied*, 2021, 15 (6), pp.064030. 10.1103/PhysRevApplied.15.064030 . insu-03744516

HAL Id: insu-03744516

<https://insu.hal.science/insu-03744516>

Submitted on 2 Sep 2022

HAL is a multi-disciplinary open access archive for the deposit and dissemination of scientific research documents, whether they are published or not. The documents may come from teaching and research institutions in France or abroad, or from public or private research centers.

L'archive ouverte pluridisciplinaire **HAL**, est destinée au dépôt et à la diffusion de documents scientifiques de niveau recherche, publiés ou non, émanant des établissements d'enseignement et de recherche français ou étrangers, des laboratoires publics ou privés.

Quantum Nondemolition Dispersive Readout of a Superconducting Artificial Atom Using Large Photon Numbers

Daria Gusenkova,^{1,2,*} Martin Spiecker,^{1,2,†} Richard Gebauer,³ Madita Willsch,⁴ Dennis Willsch,⁴ Francesco Valenti,^{1,3} Nick Karcher,³ Lukas Grünhaupt,¹ Ivan Takmakov,^{1,2,5} Patrick Winkel,^{1,2} Dennis Rieger,¹ Alexey V. Ustinov,^{1,5,6} Nicolas Roch,⁷ Wolfgang Wernsdorfer,^{1,2,8} Kristel Michielsen,⁴ Oliver Sander,³ and Ioan M. Pop^{1,2,†}

¹ PHI, Karlsruhe Institute of Technology, Karlsruhe 76131, Germany

² IQMT, Karlsruhe Institute of Technology, Eggenstein-Leopoldshafen 76344, Germany

³ IPE, Karlsruhe Institute of Technology, Eggenstein-Leopoldshafen 76344, Germany

⁴ IAS, Jülich Supercomputing Centre, Forschungszentrum Jülich, Jülich 52425, Germany

⁵ National University of Science and Technology MISIS, Moscow 119049, Russia

⁶ Russian Quantum Center, Skolkovo, Moscow 143025, Russia

⁷ Institut Néel, CNRS and Université Joseph Fourier, Grenoble, France

⁸ Université Grenoble Alpes, CNRS, Grenoble INP, Institut Néel, Grenoble 38000, France

(Received 24 November 2020; revised 19 April 2021; accepted 5 May 2021; published 11 June 2021)

Reading out the state of superconducting artificial atoms typically relies on dispersive coupling to a readout resonator. For a given system noise temperature, increasing the circulating photon number \bar{n} in the resonator enables a shorter measurement time and is therefore expected to reduce readout errors caused by spontaneous atom transitions. However, increasing \bar{n} is generally observed to also monotonously increase these transition rates. Here we present a fluxonium artificial atom in which, despite the fact that the measured transition rates show nonmonotonous fluctuations within a factor of 6, for photon numbers up to $\bar{n} \approx 200$, the signal-to-noise ratio continuously improves with increasing \bar{n} . Even without the use of a parametric amplifier, at $\bar{n} = 74$, we achieve fidelities of 99% and 93% for feedback-assisted ground and excited state preparations, respectively. At higher \bar{n} , leakage outside the qubit computational space can no longer be neglected and it limits the fidelity of quantum state preparation.

DOI: 10.1103/PhysRevApplied.15.064030

I. INTRODUCTION

Superconducting artificial atoms are among the leading platforms for the implementation of quantum information processors, due to their amenable energy spectrum and strong coupling to electromagnetic drives [1–5]. These attributes enable fast single- [6–9] and two-qubit gates [10–13], as well as high-fidelity quantum nondemolition (QND) readout [14–19]. In the circuit quantum electrodynamics architecture [2,20,21], QND readout can be achieved via dispersive coupling between a readout resonator and a superconducting artificial atom. In theory, increasing the drive of the readout resonator should improve the single-shot measurement fidelity, because the integration time can be reduced to a diminishing fraction of the artificial atom's energy relaxation time. However, increasing the readout power also introduces various

non-QND processes, such as dressed dephasing [22,23], nonlinear multimode mixing in the atom-resonator Hamiltonian [24,25], and transitions between resonant levels [26,27]. While quantitative agreement between theoretical models and experimental results is still missing, in practice, a trade-off between measurement fidelity and non-QND effects is typically reached at $\bar{n} = 1–15$ circulating photons in the resonator [28–31]. This renders Josephson parametric amplifiers with near-quantum-limited noise essential for single-shot QND readout [15,32,33].

In this paper we present a fluxonium artificial atom [34] inductively coupled to a readout antenna, which demonstrates remarkable resilience to non-QND effects up to $\bar{n} \approx 200$ readout photons. In contrast to the high-power readout reported by Reed *et al.* [35], we operate the system well below its critical photon number [20,21] $n_{\text{crit}} \approx 8 \times 10^3$ in order to minimize non-QND effects. The main difference in our design [see Fig. 1(a)] compared to previous fluxonium implementations is the use of granular aluminum (grAl) for the superinductor, coupling, and readout antenna inductances [37], replacing the conventional

* daria.gusenkova@kit.edu

† ioan.pop@kit.edu

‡ First two authors contributed equally.

arrays of mesoscopic Josephson junctions (JJs) [38,39]. Even though grAl can be modeled as an effective array of JJs [40], it operates in a distinctly different region of the parameter space: (i) its intrinsic nonlinearity can be engineered to be orders of magnitude lower compared to JJ arrays with the same inductance, and (ii) its plasma frequency is about one order of magnitude higher than that of JJ superconductors, reaching values comparable to the spectral gap of the superconductor. These changes suppress nonlinear multimode mixing, and might explain the higher resilience of the grAl fluxonium to non-QND effects at large \bar{n} when compared with JJ array fluxonions with similar spectra, which are susceptible to non-QND effects starting from $\bar{n} \approx 2$ [29].

The large readout dynamic range accessible in the grAl fluxonium enables the measurement of the photon-number-dependent dispersive shift for states $|g\rangle$ and $|e\rangle$. We show that the dispersive shift decreases with increasing readout power, as expected from the numerical diagonalization of the Hamiltonian, nevertheless, the signal-to-noise ratio (SNR) continuously improves with increasing \bar{n} . At $\bar{n} = 74$ we demonstrate 99% and 93% active state

preparation fidelities for $|g\rangle$ and $|e\rangle$, respectively, without the use of a parametric amplifier. From a practical perspective, combining a strongly nonlinear spectrum and a high-power QND readout provides a route for hardware efficient measurement in large quantum processors or superconducting detector arrays.

II. FLUXONIUM-RESONATOR CIRCUIT

A schematic of the electrical circuit used for readout and control of the fluxonium atom is shown in Fig. 1(a). The fluxonium inductively coupled to the readout resonator is fabricated on a *c*-plane sapphire chip placed inside a rectangular copper waveguide [41,42]. The readout resonator with a bare frequency $f_{r0} = 1/(2\pi\sqrt{L_r C_r}) = 7.244$ GHz, where $L_r = 22.5$ nH, has a capacitor $C_r = 21.5$ fF designed in the shape of a dipole antenna [37] that provides $\kappa/2\pi = 1.16$ MHz coupling to the microwave reflection readout setup (see Appendix B). All inductors shown in Fig. 1(a) are implemented using a 40 nm thick grAl film deposited at room temperature, with resistivity $\rho = 0.8 \times 10^3 \mu\Omega \text{ cm}$, corresponding to a sheet inductance of

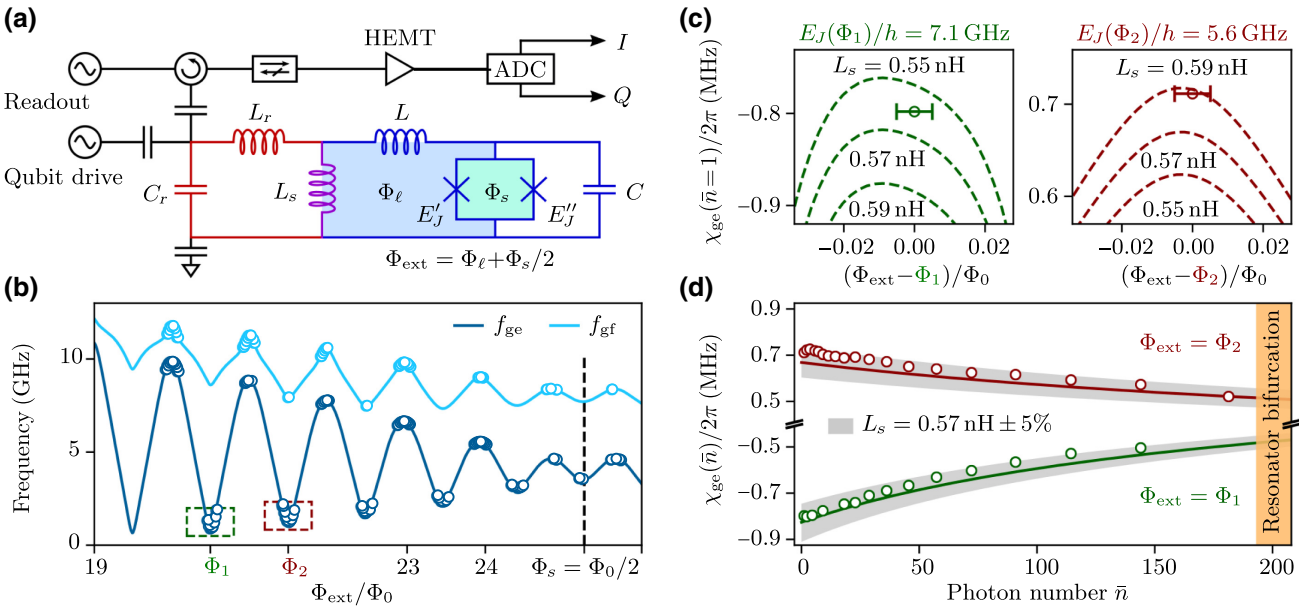


FIG. 1. Fluxonium artificial atom with *in situ* tunable Josephson energy. (a) Schematics of the measurement setup (black), readout resonator (red), and artificial atom (blue). The fluxonium consists of a superconducting quantum interference device (SQUID) junction, shunted by a superinductance $L = 231$ nH, and is dispersively coupled to the resonator via a shared inductance L_s (violet). The capacitance $C = 6.9$ fF is determined by the sum of the parallel plate capacitance of the Josephson junctions and the coplanar capacitance of the electrodes. The effective Josephson energy of the SQUID, E_J , can be tuned *in situ* by the magnetic flux Φ_s , from its maximum $E_{J+}/h = 24.0$ GHz at $\Phi_s = 0$ to its minimum $E_{J-}/h = 0.71$ GHz at the SQUID frustration $\Phi_s = \Phi_0/2$ [cf. Eq. (1)]. (b) Measured (markers) and calculated (lines) transition frequencies between the ground state $|g\rangle$ and the first (dark blue) and second (light blue) excited states, $|e\rangle$ and $|f\rangle$, respectively, versus $\Phi_{\text{ext}} = \Phi_\ell + \Phi_s/2$. (c) Dashed lines show the calculated dispersive shift $\chi_{\text{ge}}(\bar{n} = 1)/2\pi$ (MHz) in the vicinity of the two frequency minima highlighted by the green and bordeaux boxes in (b). The labels indicate the corresponding L_s values, and the markers show the measured $\chi_{\text{ge}}(\bar{n} = 1)$. Note the sign change for χ_{ge} between Φ_1 and Φ_2 . (d) Decrease of $|\chi_{\text{ge}}|$ with increasing resonator photon number \bar{n} . Markers show the measured χ_{ge} at Φ_1 (green) and Φ_2 (bordeaux). Lines indicate the calculated χ_{ge} using the values for L , C , E'_J , and E''_J extracted from the measured spectrum in Fig. 1(b), and $L_s = 0.57$ nH. The gray shaded intervals represent $L_s \pm 5\%$.

$L_{\text{kin}} = 0.1 \text{ nH}/\square$. The signal reflected from the antenna is amplified by a commercial high-electron-mobility transistor (HEMT) amplifier. At room temperature the output signal is digitized and decomposed into the I and Q quadratures by a custom designed field programmable gate array (FPGA) board [43], which allows us to implement qubit-state-dependent feedback pulses with an instrument latency of 428 ns. The measurement SNR is defined as the I - Q plane distance between $|g\rangle$ and $|e\rangle$ pointer states, divided by the sum of their standard deviations.

Following the notation in Fig. 1(a), the fluxonium Hamiltonian [34] is $H = q^2/2C + \phi^2/2L - E_J(\phi)$, where ϕ and q are the node flux and charge operators, respectively, C is the capacitance of the fluxonium JJ including the contribution of the leads, L is the superinductance, assumed to be a linear lumped element, and $E_J(\phi)$ is the equivalent Josephson energy of the fluxonium JJ implemented using a SQUID, i.e.,

$$\begin{aligned} E_J(\phi) &= \text{sgn}(E_{J+}) \sqrt{E_{J+}^2 + E_{J-}^2} \\ &\times \cos \left(\frac{2\pi}{\Phi_0} (\phi - \Phi_{\text{ext}}) - \arctan \frac{E_{J-}}{E_{J+}} \right), \end{aligned} \quad (1)$$

which is tunable via the external magnetic flux $\Phi_{\text{ext}} = \Phi_\ell + \Phi_s/2$. We use the notation $E_{J+}(\Phi_s) = (E'_J + E''_J) \cos(\pi\Phi_s/\Phi_0)$ and $E_{J-}(\Phi_s) = (E'_J - E''_J) \sin(\pi\Phi_s/\Phi_0)$, where E'_J and E''_J are the individual Josephson energies of the two JJs in the SQUID. The Hamiltonian of the fluxonium atom coupled inductively to the readout resonator is

$$\begin{aligned} H_0 &= \frac{1}{2} \phi^T \frac{1}{L_r L + L_r L_s + LL_s} \begin{pmatrix} L + L_s & -L_s \\ -L_s & L_r + L_s \end{pmatrix} \phi \\ &+ \frac{1}{2} q^T \begin{pmatrix} 1/C_r & \\ & 1/C \end{pmatrix} q - E_J(\phi), \end{aligned} \quad (2)$$

where ϕ and q are the flux and charge matrix operators, respectively. The fluxonium superinductance, readout resonator, and coupling inductances are given by L , L_r , and L_s , respectively. All inductances are considered to be linear lumped elements. Here C and C_r are the atom and the readout resonator capacitances, respectively.

III. SPECTROSCOPY

In Fig. 1(b) we show the measured (markers) and fitted (lines) fluxonium spectrum for the first three levels $|g\rangle$, $|e\rangle$, and $|f\rangle$ as a function of Φ_{ext} . We obtain the optimum SNR for resolving $|g\rangle$ and $|e\rangle$ states at two minima of the fluxonium spectrum, $\Phi_{\text{ext}} = \Phi_1$ and $\Phi_{\text{ext}} = \Phi_2$ [see Fig. 1(b)], for which $|\chi_{\text{ge}}| \approx \kappa$, where χ_{ge} is the dispersive shift of the

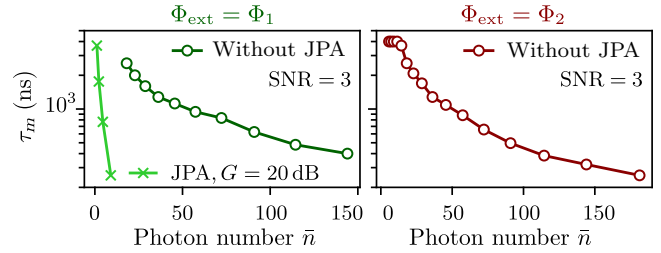


FIG. 2. Measurement time τ_m versus \bar{n} for $\text{SNR} = 3$. The data are acquired in a continuous-wave readout, without (circles) and with (crosses) the use of a parametric dimer Josephson junction array amplifier (DJAA) [44] operated at 20 dB of power gain. The Φ_{ext} values are the same as in Fig. 1.

readout resonator frequency:

$$\hbar \chi_{\text{ge}}(n) = (E_{|n+1,e\rangle} - E_{|n,e\rangle}) - (E_{|n+1,g\rangle} - E_{|n,g\rangle}). \quad (3)$$

Here $E_{|n,g\rangle}$ and $E_{|n,e\rangle}$ are the eigenenergies of the coupled fluxonium-resonator Hamiltonian [see Eq. (2)]. The dispersive shift can take both negative and positive values, as shown in Fig. 1(c) for Φ_1 and Φ_2 , respectively. We calculate the dispersive shift by numerically diagonalizing the atom-resonator Hamiltonian using the bare harmonic oscillator (Fock) basis. The Hilbert space is truncated at 20 levels for the fluxonium and $n = 220$ levels for the resonator (see Appendix C for the matrix elements of the charge and flux operators). The numerical model predicts a decrease of $|\chi_{\text{ge}}|$ with increasing \bar{n} , as observed in our measurements. In Fig. 1(d) we plot $\chi_{\text{ge}}(\bar{n})$ at $\Phi_{\text{ext}} = \Phi_1$ and $\Phi_{\text{ext}} = \Phi_2$, extracted from the measured phase shift of the resonator (see Appendices D and E). The photon number is calibrated with the ac-Stark shift of the fluxonium frequency for $\bar{n} < 15$, accounting for the $\chi_{\text{ge}}(\bar{n})$, and extrapolated linearly for higher readout power values.

The SNR's dependence with \bar{n} is the result of decreasing $\chi_{\text{ge}}(\bar{n})$ and increasing $\sqrt{\bar{n}}$:

$$\text{SNR} = \frac{\sqrt{n_m(\bar{n})}}{\sqrt{n_n/2}} \frac{2\kappa \chi_{\text{ge}}(\bar{n})}{\kappa^2 + \chi_{\text{ge}}^2(\bar{n})} \quad (4)$$

with $n_m = \bar{n}\kappa \tau_m/4$ the measurement photon number, τ_m the measurement time, and n_n the added noise photon number (see Appendix F). In our case, the SNR overall improves with increasing readout power, which is evidenced by the reduction of the measurement time required to obtain $\text{SNR} = 3$ (see Fig. 2). In combination with parametric amplification this enables the discrimination of atom states faster than the response time of the readout resonator [45].

IV. TRANSITION RATES

We perform a continuous measurement of the qubit state while the resonator is populated with \bar{n} to obtain the transition rates $\Gamma_{\uparrow}(\bar{n})$ and $\Gamma_{\downarrow}(\bar{n})$. In Fig. 3(a) we show the

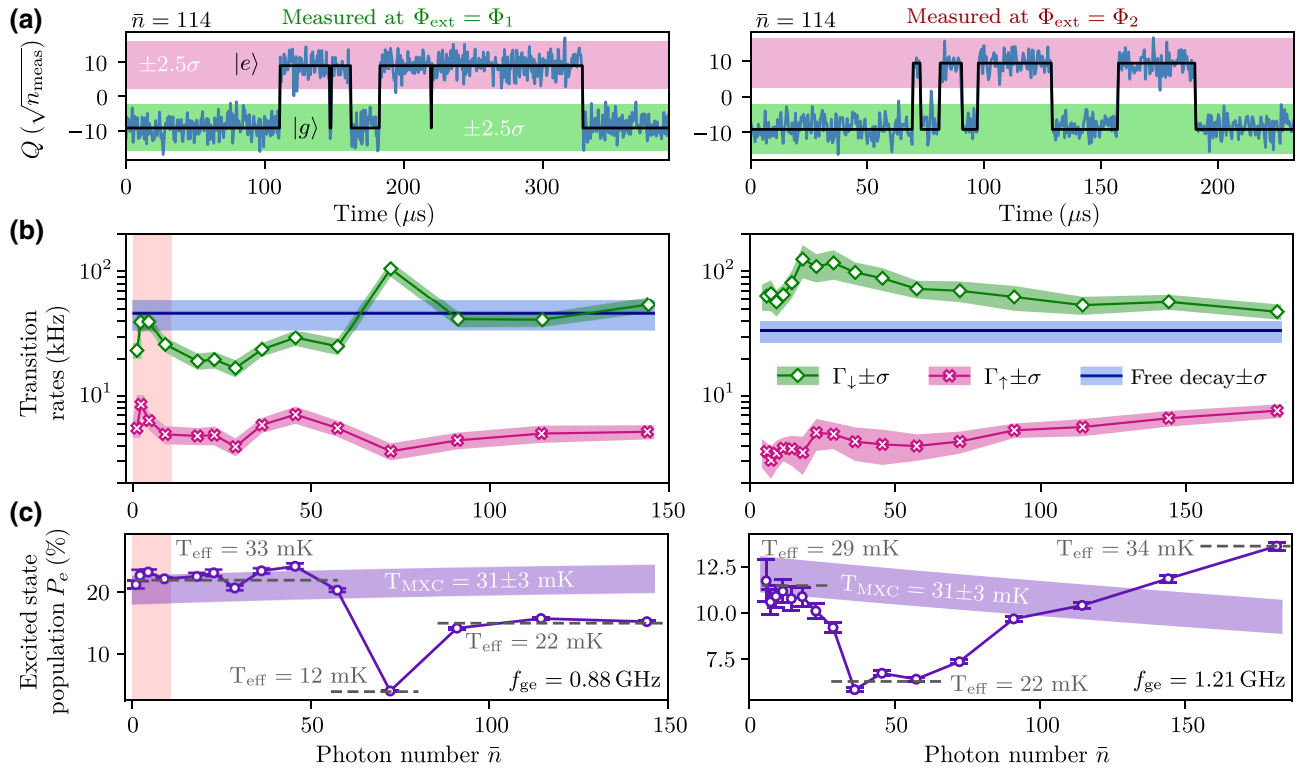


FIG. 3. Measurement of quantum jumps and qubit transition rates versus the photon number. The two columns present measurements at $\Phi_{\text{ext}} = \Phi_1$ (left) and $\Phi_{\text{ext}} = \Phi_2$ (right). (a) Typical measured time traces (blue line) of the readout resonator Q -quadrature response, without the use of a parametric amplifier, for $\bar{n} \approx 114$ circulating photons. The quadrature is rescaled to the square root of measurement photons $\sqrt{n_{\text{meas}}} = \sqrt{\bar{n}\kappa\tau_m/4}$ (see Appendix F). The measurement displays spontaneous quantum jumps of the qubit between the ground, $|g\rangle$, and excited, $|e\rangle$, states. Shaded green and pink intervals show a $\pm 2.5\sigma$ deviation from the centers of the corresponding distributions. The black lines indicate the qubit state estimation based on a two-point latching filter (see the main text). (b) Fluxonium transition rates versus \bar{n} extracted from quantum jump measurements [cf. panel (a)]: Γ_{\downarrow} (green) for $|e\rangle$ to $|g\rangle$, and Γ_{\uparrow} (crimson) for $|g\rangle$ to $|e\rangle$. The blue lines indicate the free decay rate, defined as the inverse of the energy relaxation time, measured in absence of the readout resonator drive during the atom evolution. Shaded intervals correspond to \pm one standard deviation. The pink shaded area in the left column presents the results obtained using the DJJAA using the parametric DJJAA [44], which allowed us to detect quantum jumps at small \bar{n} . (c) Excited state population (markers) versus \bar{n} ; the error bars correspond to the overlap between the histograms for $|g\rangle$ and $|e\rangle$. The shaded purple interval shows the calculated thermal occupation of the $|e\rangle$ state corresponding to the mixing chamber temperature of the dilution refrigerator, $T_{\text{MXC}} = 31 \pm 3 \text{ mK}$. Note that the qubit frequency is different at the two flux biasing points, and it depends on \bar{n} due to the ac-Stark effect. Gray labels corresponding to the dashed lines indicate the qubit effective temperature extracted from the measured $|e\rangle$ population, assuming thermal equilibrium.

measured time trace fragments (blue lines) for $\bar{n} = 114$ and $\text{SNR} = 3$, using $\tau_m = 480 \text{ ns}$ at $\Phi_{\text{ext}} = \Phi_1$ and $\tau_m = 380 \text{ ns}$ at $\Phi_{\text{ext}} = \Phi_2$. The I - Q plane is rotated such that the signal is entirely contained in the Q quadrature, and we use a two-point latching filter to assign the qubit states (black line). At each time index the filter value remains latched unless the next measured point is within a $\pm 2.5\sigma$ region centered on the other state. The histograms of time intervals spent in each state are fitted with an exponential function (see Appendix G). The resulting transition rates $\Gamma_{\uparrow}(\bar{n})$ and $\Gamma_{\downarrow}(\bar{n})$ are shown in Fig. 3(b). Note that Γ_{\downarrow} is comparable with the measured free decay rate (shown in blue) across the \bar{n} range, even though significant spikes in Γ_{\downarrow} are observed for $\bar{n} = 72$ at $\Phi_{\text{ext}} = \Phi_1$ and $\bar{n} = 18\text{--}54$ at $\Phi_{\text{ext}} = \Phi_2$. We do not observe spikes in the rates when

we perform the numerical simulations of the full system Hamiltonian. Therefore, we believe that these spikes may originate from spurious modes of the resonator and the superinductor, similar to Ref. [27].

The measured transition rates are also reflected in the fluxonium population shown in Fig. 3(c). At low photon number, for both flux bias points, the population of the excited state corresponds to a thermal excitation of the fluxonium levels in agreement with the cryostat temperature $T_{\text{MXC}} = 31 \pm 3 \text{ mK}$. With increasing \bar{n} , the expected equilibrium population changes due to the change in the frequency of the fluxonium caused by the ac-Stark shift, as indicated by the purple intervals in Fig. 3(c). Interestingly, we observe both positive and negative deviations from this trend, consistent with the measured transition

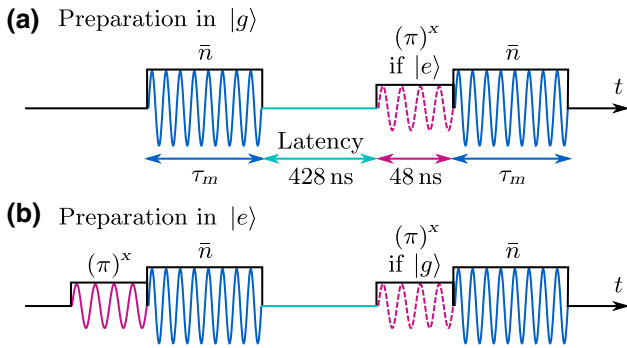


FIG. 4. Pulse sequences used for the fluxonium state preparation. (a) Preparation in the $|g\rangle$ state starts with a readout pulse of duration τ_m (shown in blue), which populates the readout resonator with \bar{n} circulating photons. Using the measured reflected signal, the fluxonium state is evaluated on-the-fly with a custom-designed FPGA-based electronics board [43]; the data processing takes 428 ns (the board latency time). A conditional π pulse (crimson dashed line) is applied if the fluxonium is measured in the $|e\rangle$ state; otherwise, the final readout pulse is played immediately after the state evaluation. The fidelity of state preparation is measured by the final readout, of the same duration and amplitude as the starting readout pulse. (b) Preparation in the excited state starts from the π pulse (crimson solid line) that inverts the thermal population of the fluxonium $|g\rangle$ and $|e\rangle$ states. The rest of the pulse sequence is analogous to that in (a), with the π pulse conditioned on the $|g\rangle$ state.

rates in Fig. 3(b). We can also extract the readout QND infidelity from the conditional probabilities to detect the same fluxonium state in two successive measurements: $1 - \mathcal{Q} = 1 - (P_{g|g} + P_{e|e})/2$ [46,47]. The QND infidelity depends on the transition rates and integration time, and it decreases with \bar{n} (see Appendix H). At $\bar{n} = 114$ we measure a QND infidelity of 2%–3%.

V. FLUXONIUM STATE PREPARATION FIDELITY

An essential figure of merit for our high photon-number dispersive readout is the process fidelity of the active fluxonium state preparation. We use a custom-designed FPGA electronics board [43] to realize the measurement-based feedback. Figure 4 depicts the pulse sequences used for the fluxonium state preparation. In Fig. 5(a) we show the measured IQ histograms at $\bar{n} = 74$ for the fluxonium before the feedback, and in Figs. 5(b) and 5(c) we plot the histograms after state preparation in $|g\rangle$ and $|e\rangle$, respectively. The state preparation fidelities are above 90% (for $|e\rangle$) and 98% (for $|g\rangle$) starting from $\bar{n} \approx 26$ up to $\bar{n} \approx 140$. Using a parametric amplifier [44] significantly reduces the measurement time and we can achieve 97% fidelity for the $|e\rangle$ state preparation.

The $|e\rangle$ state preparation histogram reveals a spurious third cloud, corresponding to the fluxonium second excited state $|f\rangle$. The extracted $|f\rangle$ state population as

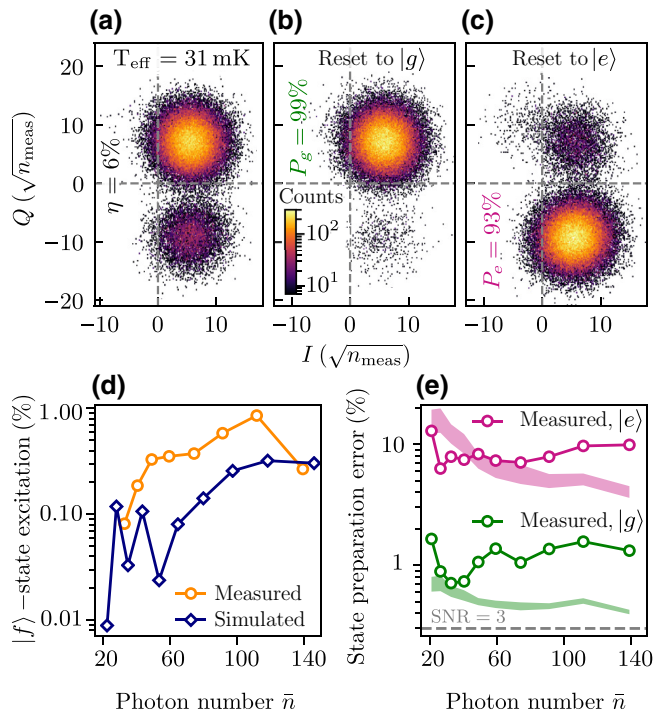


FIG. 5. Fluxonium state preparation without the use of a parametric amplifier, at $\Phi_{\text{ext}} = \Phi_2$. (a) Measured IQ histograms for $\bar{n} = 74$ and readout duration $\tau_m = 560$ ns. The Gaussian clouds correspond to steady state $|g\rangle$ and $|e\rangle$ populations measured at $\Phi_{\text{ext}} = \Phi_2$. We extract a measurement efficiency $\eta = 6\%$, corresponding to an effective noise temperature of 6.0 K (see Appendix F). (b),(c) Histograms for $|g\rangle$ and $|e\rangle$ state preparations, respectively. (d) Population of the $|f\rangle$ state. Yellow markers show values extracted from the measured IQ distributions for the $|e\rangle$ state preparation. The blue markers correspond to the values obtained by the numerical simulation of the time-dependent atom-resonator Hamiltonian with drive and dissipation for the $|e\rangle$ state preparation pulse protocol (see Appendix A). (e) Error budget for $|g\rangle$ and $|e\rangle$ state preparations. Markers show the measured errors, while the shaded intervals indicate expected errors due to transitions during the measurement and the FPGA latency time, extracted from the measured rates Γ_\uparrow and Γ_\downarrow , taking into account the $|f\rangle$ state excitation. The gray dashed line corresponds to the state discrimination error for SNR = 3.

function of \bar{n} is shown in Fig. 5(d) (markers). We simulate the $|e\rangle$ state preparation experiment by numerically calculating the time evolution of the atom-resonator system subjected to the readout drive and energy dissipation (see Appendix A). We find that the observed leakage out of the qubit computational subspace is the unintended consequence of the atom relaxation acting on the hybridized levels of the driven atom-resonator system. We emphasize that the calculated leakage to the $|f\rangle$ state [blue line in Fig. 5(d)] is 10^2 times larger than expected from thermal equilibrium. In Fig. 5(e) we show the measured (markers) state preparation errors for $|g\rangle$ and $|e\rangle$, overlaid on the expected

error intervals (shaded regions) calculated from the transition rates and the $|f\rangle$ -state leakage. Although the integration time and hence the probability of qubit state decay during readout reduces with \bar{n} , we observe that both measured and expected error values plateau. We believe that this limitation is a consequence of the increased leakage to the $|f\rangle$ state for $\bar{n} \gtrsim 70$.

VI. CONCLUSION AND OUTLOOK

In conclusion, we have demonstrated a fluxonium artificial atom for which there are significant photon-number intervals, up to $\bar{n} \approx 200$, during which the readout is QND down to the level of a few percent, similarly to the single-photon regime. The measured decrease of the dispersive shift with increasing \bar{n} is slower than the SNR improvement from the stronger readout drive; therefore, the integration time required for a given SNR decreases with \bar{n} . For $\bar{n} = 74$, we achieve state preparation fidelities of 99% for the ground state, and 93% for the excited state without the use of a parametric amplifier. We believe that the stability of the transition rates as a function of \bar{n} is a consequence of using grAl for the superinductor, coupling, and readout antenna inductances, instead of conventional JJ arrays, suppressing multimode mixing in the atom-resonator Hamiltonian. At $\bar{n} \gtrsim 70$ we identify leakage to the $|f\rangle$ state to be one of the dominant error sources. Numerical simulations indicate that this leakage is caused by spontaneous $|e\rangle$ to $|g\rangle$ transitions in the qubit undressed basis, very likely due to intrinsic losses. Future efforts will focus on improving qubit materials and design, which we expect to also reduce the $|f\rangle$ -state leakage during large \bar{n} readout.

ACKNOWLEDGMENTS

We are grateful to A. Blais, K. Borisov, D. DiVincenzo, A. Petrescu, and U. Vool for insightful discussions, and to A. Lukashenko and L. Radtke for technical support. Funding is provided by the Alexander von Humboldt foundation in the framework of a Sofja Kovalevskaja award endowed by the German Federal Ministry of Education and Research, and by the Initiative and Networking Fund of the Helmholtz Association, within the Helmholtz Future Project Scalable solid state quantum computing. M.W. and D.W. gratefully acknowledge the Gauss Centre for Supercomputing e.V. [48] for funding this project by providing computing time on the GCS Supercomputer JUWELS at Jülich Supercomputing Centre (JSC). R.G. acknowledges support by the State Graduate Sponsorship Program (LGF) and the Helmholtz International Research School for Tertronics (HIRST). A.V.U. acknowledges partial support from the Ministry of Education and Science of Russian Federation in the framework of the Increase Competitiveness Program of the National University of Science and Technology MISIS (Grant No. K2-2020-017).

APPENDIX A: NUMERICAL SIMULATION OF THE STATE PREPARATION EXPERIMENT

For the numerical simulation of the state preparation experiment, we use a time-dependent atom-resonator Hamiltonian

$$H = H_0 - E_I \sin(\omega_d t) \phi_r, \quad (\text{A1})$$

where H_0 is the static atom-resonator Hamiltonian defined in Eq. (2), and the last term describes an external time-dependent drive with amplitude E_I and frequency ω_d that represents the measurement pulse applied to the system. We perform the simulations for different values of the drive amplitude E_I to obtain steady-state photon numbers matching those observed in the experiment.

We include the dissipative effects by considering the Lindblad master equation for the time evolution of the density matrix $\rho(t)$:

$$\frac{\partial}{\partial t} \rho(t) = -i[H, \rho(t)] - \sum_{k=1,2} \left(\frac{1}{2} L_k^\dagger L_k \rho(t) + \frac{1}{2} \rho(t) L_k^\dagger L_k - L_k \rho(t) L_k^\dagger \right). \quad (\text{A2})$$

The Lindblad operator $L_1 = \sqrt{\kappa} a_r$ models the resonator decay with rate $\kappa/2\pi = 1.16$ MHz. We define the atom decay operator as $L_2 = \sqrt{\Gamma_\downarrow} \sum_j \sqrt{j} |j-1\rangle \langle j|$, where $\Gamma_\downarrow = 33.4$ kHz is the atom free decay rate measured at $\Phi_{\text{ext}} = \Phi_2$, and $|j\rangle$ denotes the j th bare atom eigenstate, obtained by diagonalizing the atom part of Eq. (A1). We

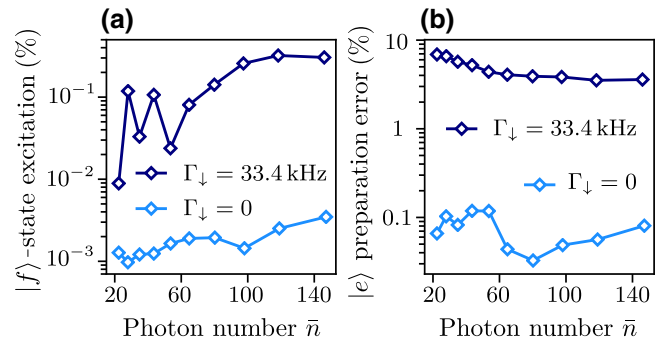


FIG. 6. Simulated error budget for the atom $|e\rangle$ state preparation. (a) Probability of the $|f\rangle$ -state excitation. The dark blue markers correspond to the simulated $|f\rangle$ -state excitation with the atom local decay $\Gamma_\downarrow = 33.4$ kHz included in the time-dependent system Hamiltonian. The light blue markers indicate $|f\rangle$ -state excitation obtained from numerical simulations without atom local decay. (b) The $|e\rangle$ state preparation error. The simulated $|e\rangle$ state preparation error with atom local decay $\Gamma_\downarrow = 33.4$ kHz (dark blue markers) is of the same order as the measured error (see Fig. 5), while excluding atom local decay (light blue markers) results in two orders of magnitude smaller errors.

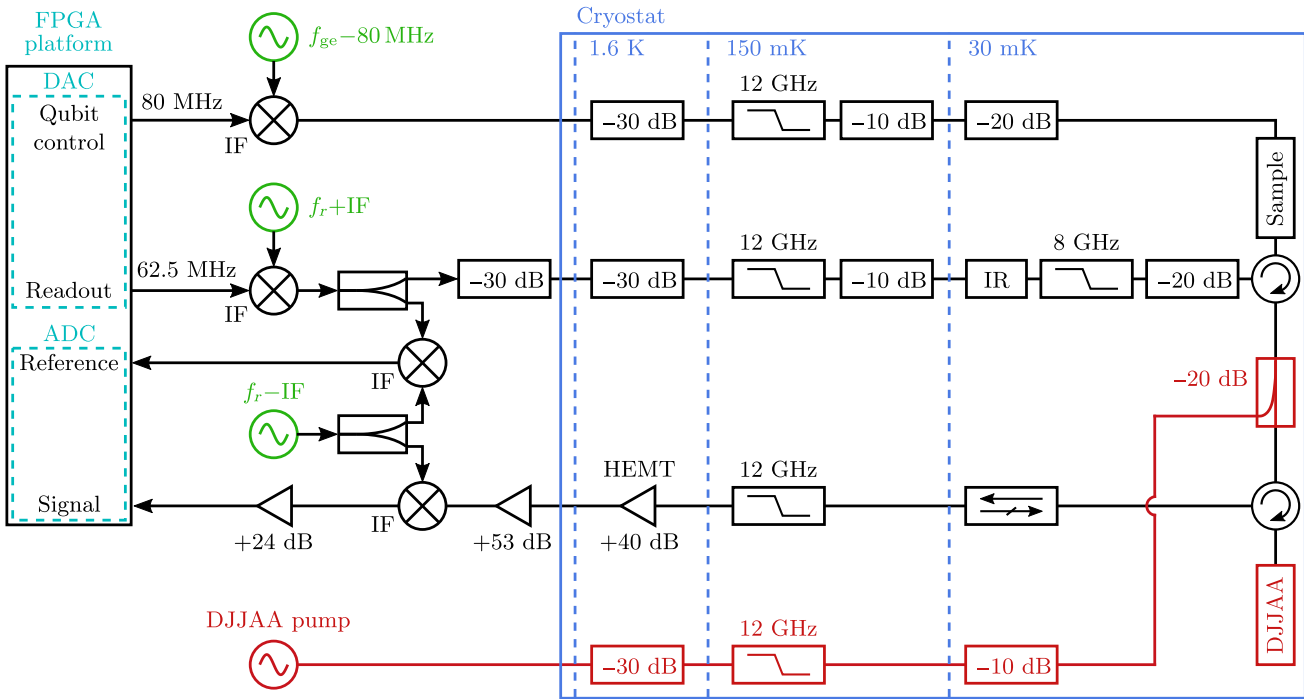


FIG. 7. Interferometric time-domain measurement setup. The digital-to-analog converter (DAC) of the custom-designed FPGA-based platform [43] generates waveforms for the readout and fluxonium control pulses, with intermediate frequencies (IF) of 62.5 and 80 MHz, respectively. The DAC waveforms are used to modulate the signals from the microwave generators (represented in green) and to convert them to the resonator frequency f_r and to the frequency of the fluxonium $|g\rangle$ - $|e\rangle$ transition. The readout line is divided into two parts. The first part of the readout tone is directly down-converted and digitized, and it serves as reference at the analog-to-digital converter (ADC) input of the FPGA. The second part of the readout tone passes through the cryostat, where the signal interacts with the sample. The signal reflected from the sample is amplified by a cascade of cryogenic and room-temperature amplifiers, down-converted, and digitized at the signal port of the ADC. The digitized *signal* and *reference* waveforms are used to calculate the I and Q quadratures of the readout resonator. To activate the parametric amplifier (DJJAA) [44], the pump tone is applied through the microwave line shown in red, connected to the signal line via a commercial directional coupler. When not pumped, the parametric DJJAA can be considered as a perfect reflector.

obtain the solution to Eq. (A2) by utilizing the wavefunction Monte Carlo method [49–51]. The calculations are performed on the supercomputer JUWELS [52] located at the Jülich Supercomputing Centre. The simulated probabilities to detect the atom in the states $|g\rangle$, $|e\rangle$, and $|f\rangle$ are averaged during same measurement time τ_m as in the experiment. These probabilities are used to calculate the expected errors for the $|e\rangle$ state preparation as a function of the readout photon numbers (see Fig. 6). We emphasize that the atom leakage out of the computational subspace, which is two orders of magnitude higher than expected from thermal population of the $|f\rangle$ state, is due to the atom relaxation acting on the hybridized levels of the driven atom-resonator system (compare the results with and without atom decay in Fig. 6).

APPENDIX B: MEASUREMENT SETUP

The measurement setup used for the feedback-assisted atom state preparation experiment is shown in Fig. 7. The sample and the parametric amplifier (DJJAA) are anchored

to the 30 mK stage of a commercial Oxford Kelvinox 100 dilution cryostat.

APPENDIX C: MATRIX ELEMENTS OF THE CHARGE AND FLUX OPERATORS

The matrix elements between states $|n, e\rangle$ and $|n, g\rangle$ of the readout resonator charge q_r , atom flux ϕ_a , and atom charge q_a operators indicate the coupling strength of the atom to dissipation channels. The calculated matrix elements are shown in Fig. 8. Remarkably, in the vicinity of the fluxonium spectra minima $\Phi_{\text{ext}} = \Phi_1$ and $\Phi_{\text{ext}} = \Phi_2$ all matrix elements do not increase with the photon number.

APPENDIX D: NONLINEARITY OF THE READOUT RESONATOR

The measured intrinsic nonlinearity of the readout resonator and calculated inherited nonlinearity due to coupling to the fluxonium atom are shown in Fig. 9.

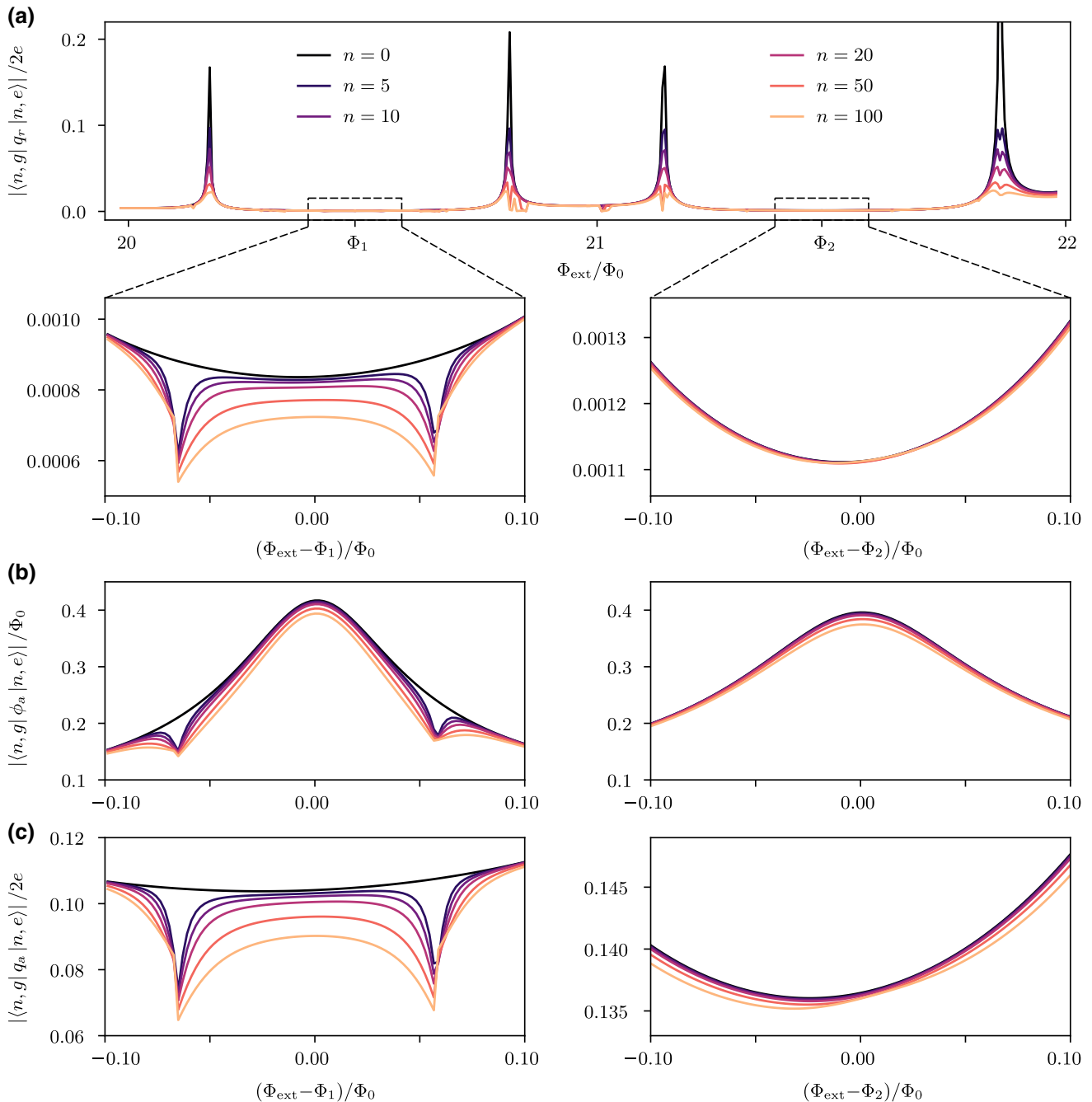


FIG. 8. Absolute value of the matrix elements between states $|n, e\rangle$ and $|n, g\rangle$ versus Φ_{ext} . Panels (a)–(c) show the matrix elements of the readout resonator charge q_r , atom flux ϕ_a , and atom charge q_a operators, respectively. The color code indicates the readout resonator photon number. The peaks of the resonator charge matrix elements [panel (a)] correspond to crossings between the levels $|0, e\rangle$ and $|1, g\rangle$, while the dips in the vicinity of $\Phi_{\text{ext}} = \Phi_1$ correspond to crossings between the levels $|1, e\rangle$ and $|0, f\rangle$.

APPENDIX E: MEASUREMENT OF THE DISPERSIVE SHIFT

The photon-number-dependent dispersive shift $\chi_{\text{ge}}(\bar{n})$ is extracted from the measured phase separation of the output $|\bar{n}, g\rangle$ and $|\bar{n}, e\rangle$ states. The phase separation is converted to a frequency shift using numerical

inversion of the calculated resonator phase response (cf. Fig. 10). We calculate the phase response as a function of the probe frequency using input-output theory [53], taking into account both intrinsic and \bar{n} -dependent inherited nonlinearity of the resonator (see Appendix D).

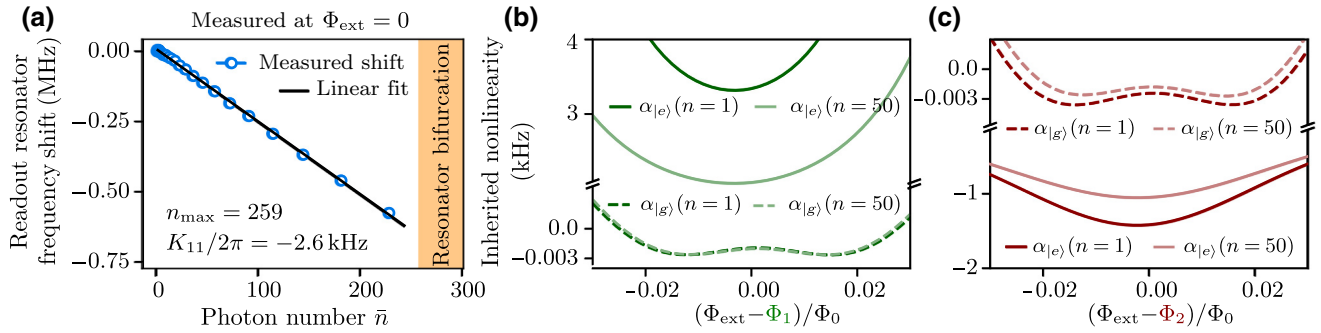


FIG. 9. Intrinsic and inherited nonlinearity of the readout resonator. (a) Frequency shift of the readout resonator versus \bar{n} (blue circle markers) solely due to the intrinsic nonlinearity of the grAl inductor [40], measured at zero external flux where the fluxonium atom is decoupled from the resonator. The black line is a linear fit. The labels indicate the self-Kerr coefficient and calculated maximal photon number at bifurcation $n_{\max} = \kappa/(\sqrt{3}K_{11})$ [53], where $\kappa/2\pi = 1.16 \text{ MHz}$ is the resonator linewidth. (b),(c) Nonlinearity of the resonator inherited from coupling to the fluxonium atom, calculated numerically in the vicinity of $\Phi_{\text{ext}} = \Phi_1$ (green lines) and $\Phi_{\text{ext}} = \Phi_2$ (bordeaux lines) from the eigenenergies of the fluxonium-resonator Hamiltonian: $\hbar\alpha_{|i\rangle}(n) = (E_{|n+1,i\rangle} - E_{|n,i\rangle}) - (E_{|n,i\rangle} - E_{|n-1,i\rangle})$ for $i = \{g, e\}$. The inherited nonlinearity is fluxonium state dependent: for the $|g\rangle$ state (dashed lines) at both flux points Φ_1 and Φ_2 , it is in the range of few hertz, while for the $|e\rangle$ state, it is orders of magnitude stronger, and it has different signs at Φ_1 and Φ_2 . The inherited nonlinearity also depends on the photon number in the resonator: green and red lines correspond to $\alpha_{|i\rangle}(n = 1)$ while faded green and faded red lines correspond to $\alpha_{|i\rangle}(n = 50)$.

APPENDIX F: IQ DISTRIBUTIONS, SIGNAL-TO-NOISE RATIO, AND MEASUREMENT EFFICIENCY

The output field operator of a driven single-port lossless resonator obeys $\hat{a}_{\text{out}}(w) = [(w - w_r - i\kappa/2)/(w - w_r$

$+ i\kappa/2)]\hat{a}_{\text{in}}(w)$ [54], where w_r is the resonator frequency, κ is the coupling rate, and $\hat{a}_{\text{in}}(w)$ is the input mode field amplitude operator. The dispersive coupling to the qubit results in a qubit-state-dependent shift of the resonator frequency $w_r = w_{r0} \pm \chi_{\text{ge}}/2$. If the resonator is driven

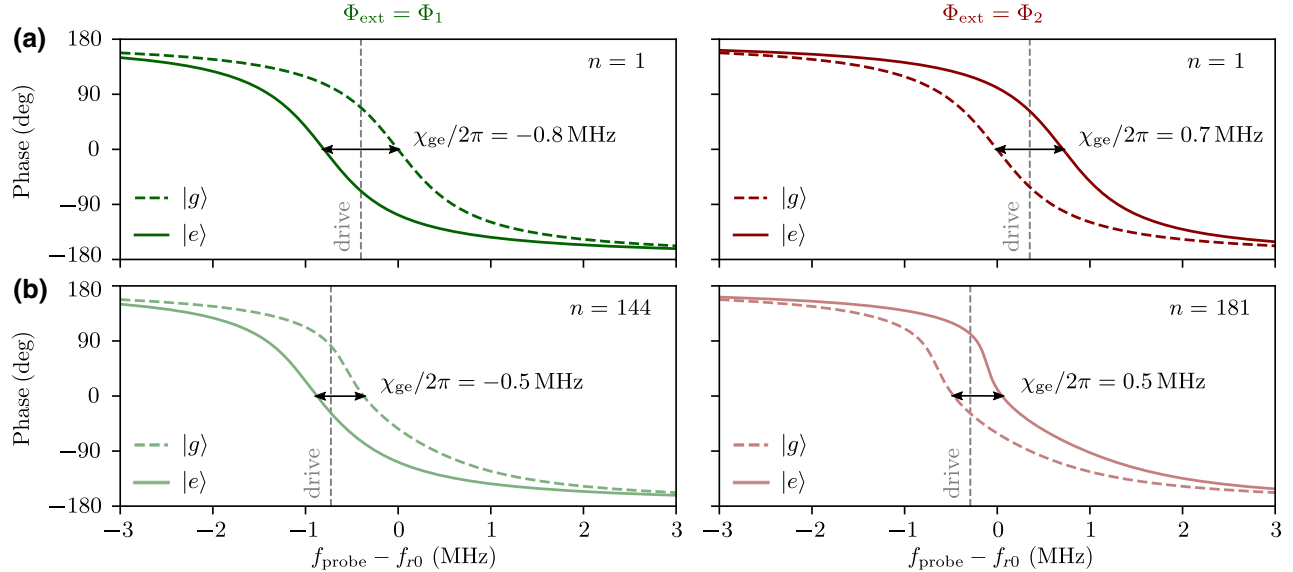


FIG. 10. Phase response of the resonator for $|g\rangle$ and $|e\rangle$ fluxonium states used to extract the dispersive shift. The phase of the signal reflected from the resonator as a function of detuning from the bare resonance frequency $f_{r0} = 7.244 \text{ GHz}$ is calculated using input-output theory [53]. The left and right columns of the figure correspond to the external flux bias points $\Phi_{\text{ext}} = \Phi_1$ and $\Phi_{\text{ext}} = \Phi_2$, respectively. The photon number is calibrated with the ac-Stark shift of the fluxonium frequency for $\bar{n} < 15$, and extrapolated linearly for higher readout power values. (a) Phase response in the single-photon regime. The dashed and solid lines correspond to the fluxonium being in the $|g\rangle$ and $|e\rangle$ states, respectively. The dashed gray lines show the readout drive frequency chosen to give the optimal phase separation between the I - Q plane pointer states. The dispersive shift is obtained by matching the maximal phase separation between the curves for $|g\rangle$ and $|e\rangle$ states to the measured phase between the I - Q plane pointer states. (b) Phase response at the highest photon number used in experiments, $\bar{n} = 144$ at $\Phi_{\text{ext}} = \Phi_1$ and $\bar{n} = 181$ at $\Phi_{\text{ext}} = \Phi_2$.

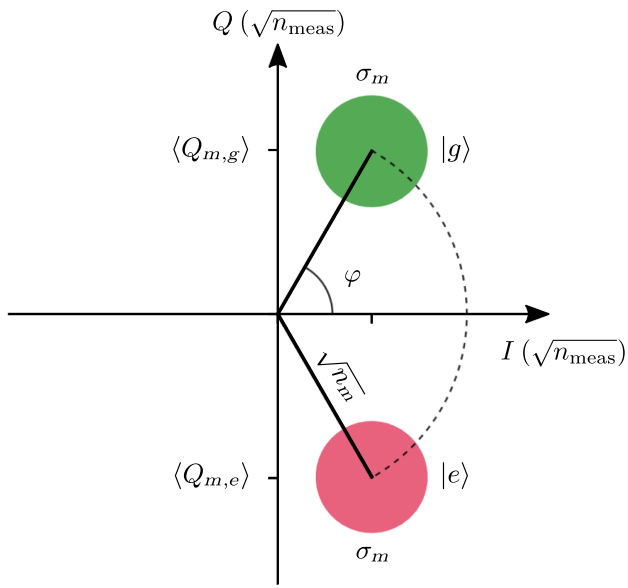


FIG. 11. Schematic IQ histogram of the integrated output signal. The I and Q quadratures are rescaled to the square root of measurement photons $\sqrt{n_{\text{meas}}} = \sqrt{\bar{n}\kappa\tau_m/4}$ [16,29]. The two disks correspond to the $|g\rangle$ and $|e\rangle$ pointer states, with identical variance $\langle(\Delta I_m)^2\rangle = \langle(\Delta Q_m)^2\rangle = \sigma_m^2$.

at the w_{r0} , the steady-state quadratures $\hat{I} = \frac{1}{2}(\hat{a}_{\text{out}}^\dagger + \hat{a}_{\text{out}})$ and $\hat{Q} = (i/2)(\hat{a}_{\text{out}}^\dagger - \hat{a}_{\text{out}})$ of the output signal

equal

$$\langle \hat{I}_{g,e} \rangle = \frac{\kappa^2 - \chi_{\text{ge}}^2}{\kappa^2 + \chi_{\text{ge}}^2} |\langle \hat{a}_{\text{in}} \rangle|, \quad \langle \hat{Q}_{g,e} \rangle = \pm \frac{2\kappa\chi_{\text{ge}}}{\kappa^2 + \chi_{\text{ge}}^2} |\langle \hat{a}_{\text{in}} \rangle|, \quad (\text{F1})$$

where the information about the qubit state is contained entirely in the Q quadrature (see Fig. 11). The output signal has to be amplified to the level accessible to the readout electronics located at room temperature. Before amplification the variance of each quadrature for the output coherent state is $\langle(\Delta I)^2\rangle = \langle(\Delta Q)^2\rangle = \frac{1}{4}$. In the ideal case, a quantum-limited phase-preserving amplifier adds a half photon of noise [54,55], which results in the total variance $\sigma_0^2 = \frac{1}{2}$ for both quadratures. The quadratures of the amplified output state are obtained using the heterodyne detection [21] and are integrated for the measurement time τ_m :

$$Q_m = \int_{t_0}^{t_0 + \tau_m} (\langle \hat{Q} \rangle + \delta Q) dt. \quad (\text{F2})$$

Here $\langle \hat{Q} \rangle$ is the quadrature expectation value according to Eq. (F1) and δQ denotes the normally distributed random noise. The integrated value I_m is obtained in a similar way. Both the average value $\langle Q_m \rangle = \langle \hat{Q} \rangle \tau_m$ and the variance $\sigma_m^2 \propto \tau_m$ of the integrated signal grow linearly

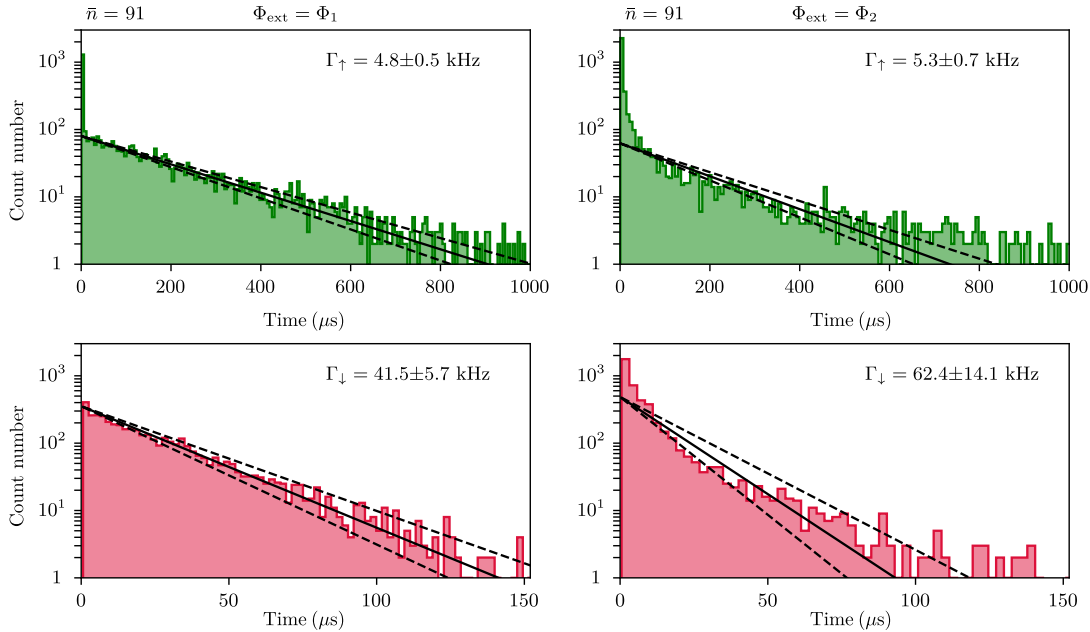


FIG. 12. Histograms of the fluxonium quantum jumps measured at $\bar{n} = 91$. The left and right columns of the figure correspond to the flux biases $\Phi_{\text{ext}} = \Phi_1$ and $\Phi_{\text{ext}} = \Phi_2$, respectively. The time intervals spent in the $|g\rangle$ (green) and $|e\rangle$ (pink) states are extracted from a continuous-wave measurement of the fluxonium using a latching filter (see the main text). The histograms contain about 5×10^3 counts. In the case of uncorrelated quantum jumps the histograms should obey a Poissonian distribution $p(\tau) = (1/\bar{\tau})e^{-\tau/\bar{\tau}}$ with the mean time $\bar{\tau}$ corresponding to the average transition rate $\Gamma = 1/\bar{\tau}$. The solid black lines show the exponential fit to the measured data, and the dashed black lines indicate the standard deviation of the extracted transition rates Γ_\uparrow and Γ_\downarrow . Note that the histograms of quantum jumps typically deviate from Poissonian statistics, similarly to the results reported in Ref. [29].

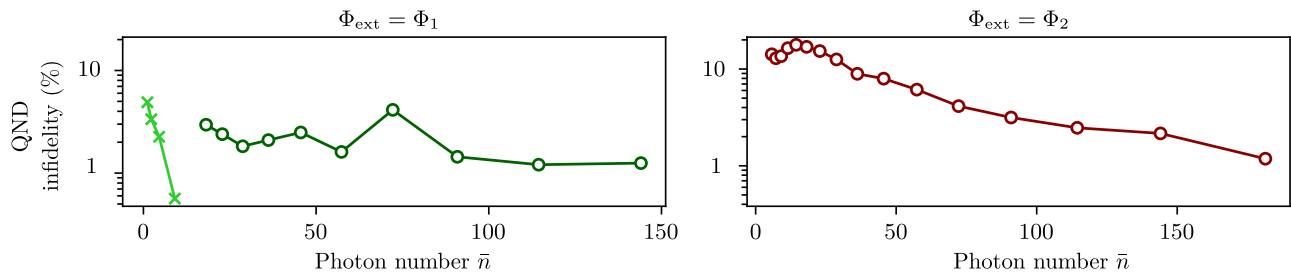


FIG. 13. QND infidelity of a continuous-wave qubit state measurement versus \bar{n} . The QND infidelity is calculated from the probability to detect the same fluxonium state in two successive measurements [46,47]: $1 - \mathcal{Q} = 1 - (P_{g|g} + P_{e|e})/2$. The integration time is chosen for each photon number according to Fig. 2 in the main text. The QND infidelity generally decreases with the photon number, directly reflecting the shorter integration time required for SNR = 3.

with the measurement time τ_m . We rescale the integrated quadratures to the square root of the measurement photons $\sqrt{n_{\text{meas}}} = \sqrt{\bar{n}\kappa\tau_m}/4$. This makes σ_m independent of the integration time, and for a quantum-limited readout, we expect $\sigma_m^2 = \frac{1}{2}$. In practice, the amplification chain is not ideal, and the added noise is higher than expected in the quantum limit. The measurement efficiency is defined as $\eta = \sigma_0^2/\sigma_m^2$ [16]. For the IQ histogram shown in Fig. 5 of the main text we obtain $\eta = 6\%$, corresponding to $n_n = 2\sigma_m^2 = 15.8$ noise photons per unit time and bandwidth, and an effective noise temperature $T_{\text{eff}} = n_n h f_r / k_B \approx 6$ K. The nominal noise temperature of the HEMT amplifier is $T \approx 2$ K.

We define the signal-to-noise ratio for the qubit state measurement as

$$\begin{aligned} \text{SNR} &= \frac{|\langle Q_{m,g} \rangle - \langle Q_{m,e} \rangle|}{\sigma_{m,g} + \sigma_{m,e}} \\ &= \frac{\sqrt{n_m}}{\sigma_m} \sin(\varphi) \\ &= \frac{\sqrt{n_m}}{\sigma_m} \frac{2\kappa\chi_{ge}}{\kappa^2 + \chi_{ge}^2}. \end{aligned} \quad (\text{F3})$$

Here $\varphi = \arctan(\langle Q_g \rangle / \langle I_g \rangle)$ is the angle formed by the pointer state associated with the qubit $|g\rangle$ state and positive real axis I_m .

APPENDIX G: MEASURED HISTOGRAMS OF THE FLUXONIUM QUANTUM JUMPS

The examples of the measured histograms of the fluxonium quantum jumps between levels $|g\rangle$ and $|e\rangle$ are shown in Fig. 12.

APPENDIX H: QND INFIDELITY

The QND infidelity of a continuous-wave qubit state measurement extracted from the fluxonium quantum jump time traces is shown in Fig. 13.

-
- [1] M. H. Devoret, S. Girvin, and R. Schoelkopf, Circuit-QED: How strong can the coupling between a Josephson junction atom and a transmission line resonator be? *Ann. Phys.* **16**, 767 (2007).
 - [2] A. Wallraff, D. I. Schuster, A. Blais, L. Frunzio, R.-S. Huang, J. Majer, S. Kumar, S. M. Girvin, and R. J. Schoelkopf, Strong coupling of a single photon to a superconducting qubit using circuit quantum electrodynamics, *Nature* **431**, 162 (2004).
 - [3] D. I. Schuster, A. A. Houck, J. A. Schreier, A. Wallraff, J. M. Gambetta, A. Blais, L. Frunzio, J. Majer, B. Johnson, M. H. Devoret, S. M. Girvin, and R. J. Schoelkopf, Resolving photon number states in a superconducting circuit, *Nature* **445**, 515 (2007).
 - [4] A. Baust, E. Hoffmann, M. Haeberlein, M. J. Schwarz, P. Eder, J. Goetz, F. Wulschner, E. Xie, L. Zhong, F. Quijandría, D. Zueco, J. J. García Ripoll, L. García-Álvarez, G. Romero, E. Solano, K. G. Fedorov, E. P. Menzel, F. Deppe, A. Marx, and R. Gross, Ultrastrong coupling in two-resonator circuit QED, *Phys. Rev. B* **93**, 214501 (2016).
 - [5] F. Yoshihara, T. Fuse, S. Ashhab, K. Kakuyanagi, S. Saito, and K. Semba, Superconducting qubit–oscillator circuit beyond the ultrastrong-coupling regime, *Nat. Phys.* **13**, 44 (2017).
 - [6] Y. Nakamura, Yu A. Pashkin, and J. S. Tsai, Coherent control of macroscopic quantum states in a single-cooper-pair box, *Nature* **398**, 786 (1999).
 - [7] J. M. Chow, L. DiCarlo, J. M. Gambetta, F. Motzoi, L. Frunzio, S. M. Girvin, and R. J. Schoelkopf, Optimized driving of superconducting artificial atoms for improved single-qubit gates, *Phys. Rev. A* **82**, 040305(R) (2010).
 - [8] Z. Chen, J. Kelly, C. Quintana, R. Barends, B. Campbell, Yu Chen, B. Chiaro, A. Dunsworth, A. G. Fowler, E. Lucero, E. Jeffrey, A. Megrant, J. Mutus, M. Neeley, C. Neill, P. J. J. O’Malley, P. Roushan, D. Sank, A. Vainsencher, J. Wenner, T. C. White, A. N. Korotkov, and John M. Martinis, Measuring and Suppressing Quantum State Leakage in a Superconducting Qubit, *Phys. Rev. Lett.* **116**, 020501 (2016).
 - [9] H. Zhang, S. Chakram, T. Roy, N. Earnest, Y. Lu, Z. Huang, D. K. Weiss, J. Koch, and D. I. Schuster, Universal

- Fast-Flux Control of a Coherent, Low-Frequency Qubit, *Phys. Rev. X* **11**, 011010 (2021).
- [10] A. O. Niskanen, K. Harrabi, F. Yoshihara, Y. Nakamura, S. Lloyd, and J. S. Tsai, Quantum coherent tunable coupling of superconducting qubits, *Science* **316**, 723 (2007).
- [11] M. A. Sillanpää, J. I. Park, and R. W. Simmonds, Coherent quantum state storage and transfer between two phase qubits via a resonant cavity, *Nature* **449**, 438 (2007).
- [12] J. Majer, J. M. Chow, J. M. Gambetta, Jens Koch, B. R. Johnson, J. A. Schreier, L. Frunzio, D. I. Schuster, A. A. Houck, A. Wallraff, A. Blais, M. H. Devoret, S. M. Girvin, and R. J. Schoelkopf, Coupling superconducting qubits via a cavity bus, *Nature* **449**, 443 (2007).
- [13] R. C. Bialczak, M. Ansmann, M. Hofheinz, M. Lenander, E. Lucero, M. Neeley, A. D. O’Connell, D. Sank, H. Wang, M. Weides, J. Wenner, T. Yamamoto, A. N. Cleland, and J. M. Martinis, Fast Tunable Coupler for Superconducting Qubits, *Phys. Rev. Lett.* **106**, 060501 (2011).
- [14] A. Lupaşcu, S. Saito, T. Picot, P. C. de Groot, C. J. P. M. Harmans, and J. E. Mooij, Quantum non-demolition measurement of a superconducting two-level system, *Nat. Phys.* **3**, 119 (2007).
- [15] R. Vijay, D. H. Slichter, and I. Siddiqi, Observation of Quantum Jumps in a Superconducting Artificial Atom, *Phys. Rev. Lett.* **106**, 110502 (2011).
- [16] M. Hatridge, S. Shankar, M. Mirrahimi, F. Schackert, K. Geerlings, T. Brecht, K. M. Sliwa, B. Abdo, L. Frunzio, S. M. Girvin, R. J. Schoelkopf, and M. H. Devoret, Quantum back-action of an individual variable-strength measurement, *Science* **339**, 178 (2013).
- [17] K. W. Murch, S. J. Weber, C. Macklin, and I. Siddiqi, Observing single quantum trajectories of a superconducting quantum bit, *Nature* **502**, 211 (2013).
- [18] P. Campagne-Ibarcq, E. Flurin, N. Roch, D. Darson, P. Morfin, M. Mirrahimi, M. H. Devoret, F. Mallet, and B. Huard, Persistent Control of a Superconducting Qubit by Stroboscopic Measurement Feedback, *Phys. Rev. X* **3**, 021008 (2013).
- [19] U. Vool, S. Shankar, S. O. Mundhada, N. Ofek, A. Narla, K. Sliwa, E. Zalys-Geller, Y. Liu, L. Frunzio, R. J. Schoelkopf, S. M. Girvin, and M. H. Devoret, Continuous Quantum Nondemolition Measurement of the Transverse Component of a Qubit, *Phys. Rev. Lett.* **117**, 133601 (2016).
- [20] A. Blais, R.-S. Huang, A. Wallraff, S. M. Girvin, and R. J. Schoelkopf, Cavity quantum electrodynamics for superconducting electrical circuits: An architecture for quantum computation, *Phys. Rev. A* **69**, 062320 (2004).
- [21] A. Blais, A. L. Grimsmo, S. M. Girvin, and A. Wallraff, Circuit quantum electrodynamics, *ArXiv:2005.12667* (2020).
- [22] M. Boissonneault, J. M. Gambetta, and A. Blais, Nonlinear dispersive regime of cavity QED: The dressed dephasing model, *Phys. Rev. A* **77**, 060305(R) (2008).
- [23] M. Boissonneault, J. M. Gambetta, and A. Blais, Dispersive regime of circuit QED: Photon-dependent qubit dephasing and relaxation rates, *Phys. Rev. A* **79**, 013819 (2009).
- [24] M. Malekakhlagh, A. Petrescu, and H. E. Türeci, Lifetime renormalization of weakly anharmonic superconducting qubits. I. Role of number nonconserving terms, *Phys. Rev. B* **101**, 134509 (2020).
- [25] A. Petrescu, M. Malekakhlagh, and H. E. Türeci, Lifetime renormalization of driven weakly anharmonic superconducting qubits. II. The readout problem, *Phys. Rev. B* **101**, 134510 (2020).
- [26] D. H. Slichter, R. Vijay, S. J. Weber, S. Boutin, M. Boissonneault, J. M. Gambetta, A. Blais, and I. Siddiqi, Measurement-Induced Qubit State Mixing in Circuit QED from Up-Converted Dephasing Noise, *Phys. Rev. Lett.* **109**, 153601 (2012).
- [27] D. Sank, *et al.*, Measurement-Induced State Transitions in a Superconducting Qubit: Beyond the Rotating Wave Approximation, *Phys. Rev. Lett.* **117**, 190503 (2016).
- [28] J. E. Johnson, C. Macklin, D. H. Slichter, R. Vijay, E. B. Weingarten, J. Clarke, and I. Siddiqi, Heralded State Preparation in a Superconducting Qubit, *Phys. Rev. Lett.* **109**, 050506 (2012).
- [29] U. Vool, I. M. Pop, K. Sliwa, B. Abdo, C. Wang, T. Brecht, Y. Y. Gao, S. Shankar, M. Hatridge, G. Catelani, M. Mirrahimi, L. Frunzio, R. J. Schoelkopf, L. I. Glazman, and M. H. Devoret, Non-Poissonian Quantum Jumps of a Fluxonium Qubit Due to Quasiparticle Excitations, *Phys. Rev. Lett.* **113**, 247001 (2014).
- [30] T. Walter, P. Kurpiers, S. Gasparinetti, P. Magnard, A. Potočnik, Y. Salathé, M. Pechal, M. Mondal, M. Oppliger, C. Eichler, and A. Wallraff, Rapid High-Fidelity Single-Shot Dispersive Readout of Superconducting Qubits, *Phys. Rev. Appl.* **7**, 054020 (2017).
- [31] Z. K. Minev, S. O. Mundhada, S. Shankar, P. Reinhold, R. Gutiérrez-Jáuregui, R. J. Schoelkopf, M. Mirrahimi, H. J. Carmichael, and M. H. Devoret, To catch and reverse a quantum jump mid-flight, *Nature* **570**, 200 (2019).
- [32] M. A. Castellanos-Beltran, K. D. Irwin, G. C. Hilton, L. R. Vale, and K. W. Lehnert, Amplification and squeezing of quantum noise with a tunable Josephson metamaterial, *Nat. Phys.* **4**, 929 (2008).
- [33] N. Bergeal, F. Schackert, M. Metcalfe, R. Vijay, V. E. Manucharyan, L. Frunzio, D. E. Prober, R. J. Schoelkopf, S. M. Girvin, and M. H. Devoret, Phase-preserving amplification near the quantum limit with a Josephson ring modulator, *Nature* **465**, 64 (2010).
- [34] V. E. Manucharyan, J. Koch, L. I. Glazman, and M. H. Devoret, Fluxonium: Single cooper-pair circuit free of charge offsets, *Science* **326**, 113 (2009).
- [35] M. D. Reed, L. DiCarlo, B. R. Johnson, L. Sun, D. I. Schuster, L. Frunzio, and R. J. Schoelkopf, High-Fidelity Readout in Circuit Quantum Electrodynamics Using the Jaynes-Cummings Nonlinearity, *Phys. Rev. Lett.* **105**, 173601 (2010).
- [36] W. C. Smith, A. Kou, U. Vool, I. M. Pop, L. Frunzio, R. J. Schoelkopf, and M. H. Devoret, Quantization of inductively shunted superconducting circuits, *Phys. Rev. B* **94**, 144507 (2016).
- [37] L. Grünhaupt, M. Spiecker, D. Gusenkova, N. Maleeva, S. T. Skael, I. Takmakov, F. Valenti, P. Winkel, H. Rotzinger, W. Wernsdorfer, A. V. Ustinov, and Ioan M. Pop, Granular aluminium as a superconducting material for high-impedance quantum circuits, *Nat. Mater.* **18**, 816 (2019).

- [38] M. T. Bell, I. A. Sadovskyy, L. B. Ioffe, A. Yu Kitaev, and M. E. Gershenson, Quantum Superinductor with Tunable Nonlinearity, *Phys. Rev. Lett.* **109**, 137003 (2012).
- [39] N. A. Masluk, I. M. Pop, A. Kamal, Z. K. Minev, and M. H. Devoret, Microwave Characterization of Josephson Junction Arrays: Implementing a Low Loss Superinductance, *Phys. Rev. Lett.* **109**, 137002 (2012).
- [40] N. Maleeva, L. Grünhaupt, T. Klein, F. Levy-Bertrand, O. Dupre, M. Calvo, F. Valenti, P. Winkel, F. Friedrich, W. Wernsdorfer, A. V. Ustinov, H. Rotzinger, A. Monfardini, M. V. Fistul, and I. M. Pop, Circuit quantum electrodynamics of granular aluminum resonators, *Nat. Commun.* **9**, 3889 (2018).
- [41] L. Grünhaupt, N. Maleeva, S. T. Skacel, M. Calvo, F. Levy-Bertrand, A. V. Ustinov, H. Rotzinger, A. Monfardini, G. Catelani, and I. M. Pop, Loss Mechanisms and Quasiparticle Dynamics in Superconducting Microwave Resonators Made of Thin-Film Granular Aluminum, *Phys. Rev. Lett.* **121**, 117001 (2018).
- [42] A. Kou, W. C. Smith, U. Vool, I. M. Pop, K. M. Sliwa, M. Hatridge, L. Frunzio, and M. H. Devoret, Simultaneous Monitoring of Fluxonium Qubits in a Waveguide, *Phys. Rev. Appl.* **9**, 064022 (2018).
- [43] R. Gebauer, N. Karcher, D. Gusekova, M. Spiecker, L. Grünhaupt, I. Takmakov, P. Winkel, L. Planat, N. Roch, W. Wernsdorfer, A. V. Ustinov, M. Weber, M. Weides, I. M. Pop, and O. Sander, State preparation of a fluxonium qubit with feedback from a custom fpga-based platform, *AIP Conf. Proc.* **2241**, 020015 (2020).
- [44] P. Winkel, I. Takmakov, D. Rieger, L. Planat, W. Hasch-Guichard, L. Grünhaupt, N. Maleeva, F. Foroughi, F. Henriques, K. Borisov, J. Ferrero, A. V. Ustinov, W. Wernsdorfer, N. Roch, and I. M. Pop, Nondegenerate Parametric Amplifiers Based on Dispersion-Engineered Josephson-Junction Arrays, *Phys. Rev. Appl.* **13**, 024015 (2020).
- [45] I. Takmakov, P. Winkel, F. Foroughi, L. Planat, D. Gusekova, M. Spiecker, D. Rieger, L. Grünhaupt, A. V. Ustinov, W. Wernsdorfer, I. M. Pop, and N. Roch, Minimizing the Discrimination Time for Quantum States of an Artificial Atom, *Phys. Rev. Appl.* **15**, 064029 (2021).
- [46] R. Dassonneville, T. Ramos, V. Milchakov, L. Planat, É. Dumur, F. Foroughi, J. Puertas, S. Leger, K. Bharadwaj, J. Delaforce, C. Naud, W. Hasch-Guichard, J. J. García Ripoll, N. Roch, and O. Buisson, Fast High-Fidelity Quantum Nondemolition Qubit Readout Via a Nonperturbative Cross-Kerr Coupling, *Phys. Rev. X* **10**, 011045 (2020).
- [47] S. Touzard, A. Kou, N. E. Frattini, V. V. Sivak, S. Puri, A. Grimm, L. Frunzio, S. Shankar, and M. H. Devoret, Gated Conditional Displacement Readout of Superconducting Qubits, *Phys. Rev. Lett.* **122**, 080502 (2019).
- [48] <https://www.gauss-centre.eu/>.
- [49] J. Dalibard, Y. Castin, and K. Mølmer, Wave-Function Approach to Dissipative Processes in Quantum Optics, *Phys. Rev. Lett.* **68**, 580 (1992).
- [50] R. Dum, P. Zoller, and H. Ritsch, Monte Carlo simulation of the atomic master equation for spontaneous emission, *Phys. Rev. A* **45**, 4879 (1992).
- [51] Kurt Jacobs, *Quantum Measurement Theory and its Applications* (Cambridge University Press, Cambridge, 2014).
- [52] Jülich Supercomputing Centr, Juwels: Modular tier-0/1 supercomputer at the Jülich supercomputing centre, *J. Large-Scale Res. Facil.* **5**, A135 (2019).
- [53] C. Eichler and A. Wallraff, Controlling the dynamic range of a Josephson parametric amplifier, *EPJ Quantum Technol.* **1**, 2 (2014).
- [54] A. A. Clerk, M. H. Devoret, S. M. Girvin, F. Marquardt, and R. J. Schoelkopf, Introduction to quantum noise, measurement, and amplification, *Rev. Mod. Phys.* **82**, 1155 (2010).
- [55] Carlton M. Caves, Quantum limits on noise in linear amplifiers, *Phys. Rev. D* **26**, 1817 (1982).